Author Manuscript

Author Manuscript

Author Manuscript

Author Manuscript

HHS Public Access

Author manuscript

Anal Chem. Author manuscript; available in PMC 2021 August 04.

Published in final edited form as:

Anal Chem. 2020 August 04; 92(15): 10751–10758. doi:10.1021/acs.analchem.0c02104.

Interplay of Effective Surface Area, Mass Transport, and Electrochemical Features in Nanoporous Nucleic Acid Sensors

Jovana Veselinovic[1,‡], **Suzan AlMashtoub**[1,‡], **Sachit Nagella**[1,‡], **Erkin Seker**[2,*]

[1]Department of Chemical Engineering, University of California - Davis, Davis, California 95616, United States

[2]Department of Electrical and Computer Engineering, University of California - Davis, Davis, California 95616, United States

Abstract

Electrochemical biosensors transduce biochemical events (e.g., DNA hybridization) to electrical signals and can be readily interfaced with electronic instrumentation for portability. Nanostructuring the working electrode enhances sensor performance via augmented effective surface area that increases the capture probability of an analyte. However, increasing the effective surface area via thicker nanostructured electrodes hinders the analyte's permeation into the nanostructured volume and limits its access to deeper electrode surfaces. Here, we use nanoporous gold (np-Au) with various thicknesses and pore morphologies coupled with methylene blue (MB) reporter-tagged DNA probe for DNA target detection, as a model system, to study the influence of electrode features on electrochemical sensing performance. Independent of the DNA target concentration, the hybridization current (surrogate for detection sensitivity) increases with the surface enhancement factor (EF), until an EF of ~ 5, after which the sensor performance deteriorates. Electrochemical and fluorometric quantification of desorbed DNA probe suggest that DNA permeation is severely limited for higher EFs. In addition, undesirable capacitive currents disguise the faradaic currents from the MB reporter at larger EFs that require higher square wave voltammetry (SWV) frequencies. Finally, a real-time hybridization study reveals that expanding the effective surface area beyond EFs around 5, decreases sensor performance.

GRAPHICAL ABSTRACT

*Corresponding author Phone: 530-752-7300. eseker@ucdavis.edu.

‡These authors contributed equally.

Author Contributions

All authors designed the experiments; JV, SN, and SA collected; all authors analyzed/interpreted the data; and all authors contributed to writing the manuscript and have given approval to the final version of the manuscript.

Supporting Information

The Supporting Information is available free of charge on the ACS Publications website at DOI: electrode fabrication details, electrochemical and microscopic characterization, optimization of hybridization conditions, supplemental plots to figures 3 and 5, relative probe currents at optimized frequencies, example of SWV baseline shifts, electrochemical impedance spectroscopy, real-time hybridization data (PDF).

The authors declare no competing financial interest.

Author Manuscript Author Manuscript Author Manuscript Author Manuscript

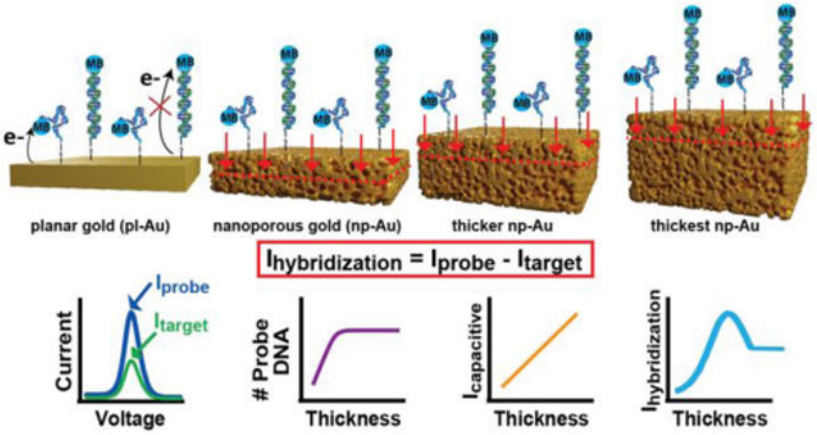

Electrochemical biosensors are powerful bioanalytical tools that are emerging in many applications (e.g., clinical, environmental, industrial, pharmaceutical, defense, etc.), due to their simplicity and cost, excellent limits of detection[1], ease of integration with electronic instrumentation[2], and amenability to miniaturization[3], multiplexing[4], and portability[5]. The biophysical interface, that is, the working electrode functionalized with a molecular recognition layer for a specific target analyte, plays a critical role in the sensor performance[6]. Even though the recognition layer can consist of various biomolecular elements, such as enzymes and antibodies[7], nucleic acids have been gaining significance as both, the target and recognition layer (capture probe). The reasons include nucleic acids' high selectivity for specific targets, reversible binding to a wide variety of molecular targets (e.g., ions[8], small molecules[9], proteins[10], whole cells[11]), ease of custom synthesis[12], and high tolerance to storage temperature variations[13]. Similarly, the working electrode that supports the recognition layer and interfaces it to electronics plays an equally vital role in electrochemical biosensor performance. Nanostructuring the working electrode with different material architectures (e.g., carbon nanotubes[14], gold nanorods[15], palladium dendritic nanostructures[10]) generally enhances electrochemical sensor performance[17-20] via several mechanisms, including an increased number of capture probes per electrode volume that increases the probability of capturing analytes and leverages unique nanoscale transport phenomena[17,21,22]. These beneficial features have driven interest in implementing porous and dendritic structures as working electrode thin-film coatings in electrochemical sensors. Thicker porous films increase effective surface area of the working electrode (referred to as enhancement factor (EF), or the ratio of the porous film electrochemically-active surface area to that of a smooth electrode). Increasing the effective surface area (assuming no transport limitations) by increasing electrode thickness would increase the number of capture probes, and thereby increase the probability of target DNA capture, and in turn, enhance target detection capability of the sensor. EHowever, for thicker porous electrodes, there is a mass transport efficiency trade-off, where the permeation of analytes into the pores is hindered. The competition between these two factors (effective surface area and mass transport limitations) largely dictate the overall sensor performance[23]. Here, we use nanoporous gold (np-Au) functionalized with DNA capture probes as a model working electrode system. The np-Au electrode coatings have shown to increase dynamic range[22,24]

Author Manuscript Author Manuscript Author Manuscript Author Manuscript

and selectivity[25], as well as improve biofouling tolerance[26] of electrochemical nucleic acid sensors. In addition, np-Au thin films can be produced and patterned by conventional microfabrication techniques and the pore morphology can precisely be tuned by thermal annealing[27]. Enabled with these features of np-Au thin films, the objective of this study is to provide insight into the influence of working electrode features on DNA-based electrochemical sensing performance, by systematically varying pore morphology and film thickness of np-Au thin-film electrodes to obtain a wide range of effective surface. Here, we define sensor performance metric as the difference in peak current relative to the baseline between the probe and target signal, expressed as *hybridization current change* (Figure 1). More specifically, the study consists of the following complementary parts: (i) electrochemical evaluation of sensor's performance for a wide range of EFs; (ii) electrochemical and fluorometric characterization of the DNA capture probe layer; (iii) investigation of the key electrochemical interrogation parameters (e.g., square wave voltammetry frequency); and (iv) a real-time hybridization study to reveal transport effects and optimal nanoporous working electrode thickness.

EXPERIMENTAL SECTION

Chemical Reagents.

Electron Microscopy Sciences glass coverslips were used as substrates for film deposition (22 x 22 x 0.15 mm). Gold (Au), silver (Ag), and chrome (Cr) targets (99.95% pure) were obtained from Kurt J. Lesker. Nitric acid (70%), sulfuric acid (96%), and hydrogen peroxide (30%) were purchased from Sigma-Aldrich, USA. Piranha solution consisted of 1:4 ratio (by volume) of hydrogen peroxide and sulfuric acid. CAUTION: *Piranha solution and nitric acid are highly corrosive and reactive with organic materials and must be handled with extreme care*. Tris(2-chloroethyl)phosphate (TCEP, 0.5 M), magnesium chloride ($MgCl_2$, powder) and phosphate buffer (PB, 1 M) were obtained from Fisher Scientific. Phosphate buffered saline (PBS, 10×) was purchased from Life Technologies. Zeba™ Spin Desalting Columns were obtained from Thermo Fisher Scientific. The oligonucleotides used in this project consisted of 26 bases and were purchased from Integrated DNA Technologies, USA. The 5′ end of single-stranded DNA (ssDNA) MB-tagged probe was modified with a C6 linker and thiol group, while 3' end was modified with Methylene Blue (MB) as a redox reporter of the system: /5ThioMC6-D/CGT GTT ATA AAA TGT AAT TTG GAA TT/3MeBIN/. Single-stranded Target DNA sequence matching to the DNA probe was: AAT TCC AAA TTA CAT TTT ATA ACA CG. Quant-iT™ OliGreen™ ssDNA Assay Kit was obtained from Thermo Fisher Scientific.

Fabrication of Nanoporous Gold (np-Au) Electrodes.

The np-Au gold films of various thickness were prepared by varying sputter-deposition time (i.e., 5, 10, 20, 30 minutes) of the $Au_{0.36}Ag_{0.64}$ (atomic %) alloy on top of 160 nm-thick chrome adhesion layer and 80 nm-thick gold seed layer pre-deposited on the piranha-cleaned glass coverslips, using a previously established deposition protocol[22]. All sputter-coated alloy thin films are dealloyed in the nitric acid at 55°C[28], generating set of *unannealed np-Au* samples with four different thicknesses. A set of each of the generated samples was thermally treated at 250 °C for 1.5 min on a hotplate[25], generating four

Author Manuscript Author Manuscript Author Manuscript Author Manuscript

additional thicknesses with coarser morphology (*annealed np-Au*). Planar gold electrodes (control morphology) were fabricated similarly. Fabrication details can be found in Supporting Information (SI).

Microscopic and Electrochemical Characterization of Electrode Morphology.

To investigate micro- and nano-scale morphological features of the fabricated samples, high-magnification images (100k× magnification) were taken using scanning electron microscopy (SEM; FEI Nova NanoSEM430) to obtain top-view images. The top views of varying electrode morphology and thickness samples were analyzed using ImageJ (National Institutes of Health shareware, http://rsb.info.nih.gov/ij/index.html) in order to determine the median pore size[29]. To determine thickness of each representative sample set, a FEI Scios Dual Beam FIB/SEM was used. The cross sections were obtained by cutting into the sample surface using a gallium focused ion beam and were imaged simultaneously with a scanning electron microscope.

All electrochemical experiments were performed with a Gamry Reference 600 potentiostat. Effective surface area of the gold electrodes was determined using electrochemical cyclic voltammetry (CV) measurements using previously established protocols that report on the charge required to strip the gold oxide layer via CV[30,31], when using 0.5 M sulfuric acid. For all the measurements, enhancement factor (EF) is defined as the ratio of effective surface area measured for any test morphology to that for pl-Au under the same testing conditions.

Immobilization of the MB-tagged DNA Probe Capture Layer.

Eight different types of electrodes (4 thicknesses of unannealed and 4 thicknesses of annealed np-Au, all n = 3) were used. Note that for the entire study, four identical sets of such electrodes were prepared using previously described grafting protocols that consisted of incubating the working electrode overnight (~15 hours) with 0.5 μM MB-tagged DNA probe solution prepared in 25 mM PB and 50 mM $MgCl_2$[2232]. To obtain a well-ordered DNA probe monolayer, electrodes were backfilled with MCH, as routinely used[33-35]. Finally, the DNA probe-functionalized electrode was assembled in the electrochemical cell for electrochemical characterization (Figure S1).

Electrochemical Evaluation of Sensor Performance at Various EFs and Morphologies.

To evaluate sensor performance, quantified through the hybridization current change as a measure of target detection capability, it is necessary to first electrochemically quantify the amount of DNA probe immobilized on the electrodes, via the *relative probe current* (Figure 1). Electrochemically-active surface area of the immobilized MB-tagged probes was acquired in 1× PBS using square wave voltammetry (SWV) measurements for all 8 types of electrodes (n = 3). The SWV relative probe current was determined directly from Gamry Software and used as an indirect measure of the amount of DNA probe immobilization on the electrode surfaces. SWV was performed using a pulse size of 40 mV and frequency previously optimized for different electrode morphologies: 18 Hz for unannealed np-Au, 30 Hz for annealed np-Au, and 60 Hz for pl-Au[22]. After the relative probe current signal determination, all electrodes were challenged with four different target DNA concentrations (250, 500, 1000, 4000 nM) to determine the sensor performance in detecting the DNA

Author Manuscript Author Manuscript Author Manuscript Author Manuscript

analytes. Each electrode was incubated in 1x PBS containing the target DNA fragments for 15 min at room temperature (RT), as shown in Figure S1. The electrodes were then rinsed to remove nonspecifically bound target molecules. Amount of target DNA captured by the probe recognition layer can be determined by the difference between the *probe peak current* and *target peak current*[36] (Figure 1). The difference in SWV *peak current* relative to the baseline between the probe and target was used to quantify the hybridization events in each case, expressed as *hybridization current change*, which is classified as a 'signal-off electrochemical detection mode (Figure 1). See Figure S1 for the electrochemical cell and operation mechanism description.

Electrochemical and Fluorometric Characterization of the Capture Probe Layer.

To understand the effect of DNA probe capture layer on overall sensor performance, eight types of representative immobilized electrodes (n = 3) were tested to obtain SWV peak current due to MB-tagged DNA probe at previously mentioned optimal frequencies and SWV parameters. The immobilized DNA probes were electrochemically eluted for fluorometric determination of the amount of DNA probe, using a previously-established protocol ensuring efficient extraction of immobilized DNA from the pores[37,38].

Electrochemical Extraction and Fluorometric Analysis of DNA Probe-Immobilized Electrodes.

To decouple the influence of electrochemical effects, which would obscure the determination of actual immobilized probe amount, an independent measurement with fluorescent dyes was used on the electrochemically-extracted DNA probes[39,40]. To fluorometrically quantify the amount of DNA probes, extracted DNA probe solution was analyzed using Quant-iT™ OliGreen™ ssDNA Kit. Briefly, OliGreen dye was added to the extracted samples, and after 5 minutes of incubation at room temperature, a NanoDrop™ Spectrophotometer was used for quantifying the amount of DNA present in the extracted samples.

Frequency Optimization for the Capture Probe Layer.

DNA probe-functionalized electrodes were used to determine the optimal SWV frequency that maximizes the relative probe current. Each electrode was tested at various SWV frequencies (3, 10, 18, 25, 30 and 40 Hz) and SWV relative probe current was measured.

Impedance Measurements.

To approximate the extent of MCH passivation in the np-Au electrodes, electrical double layer capacitance C_{dl} was extracted from electrochemical impedance spectroscopy (EIS) of the DNA probe-functionalized electrodes with the highest and lowest EFs. The EIS Nyquist plots were obtained for the frequency range of 0.3 - 10,000 Hz in 1× PBS. A Randles equivalent circuit with a Warburg element was modeled with a built-in model editor in Gamry Software (Figure S9) and used to fit the EIS data to obtain C_{dl} and electrolyte resistance (R_s) for comparison with previous studies.

Author Manuscript Author Manuscript Author Manuscript Author Manuscript

Real-time Hybridization of Target DNA.

To investigate the hybridization kinetics of target DNA when introduced to electrodes of various thicknesses, DNA probe-functionalized electrodes were used. First, the SWV DNA relative probe current signal was acquired as described above. Next, all the electrodes were challenged with four different target DNA concentrations (250, 500, 1000, 4000 nM). Each electrode was incubated with the target DNA fragments in 1× PBS at room temperature and SWV signal was recorded at previously determined optimal frequencies to determine the extent of hybridization at the given time point (0, 1, 2, 3, 5, 7, 9, 12 and 15 minutes). The samples with EF = 27.9 and 36.1 were not used for this part of the study, since their relative probe current signal could not be optimized, reasons for which are described in Results and Discussion.

RESULTS AND DISCUSSION

Electrode Characterization.

Selective dissolution of silver atoms in nitric acid and surface diffusion of gold atoms at the metal electrolyte interface, which is the process of *dealloying*, results in a bicontinuous open-pore structure[41]. Typically, the residual silver in the final np-Au electrodes is less than 5% (atomic %)[42] and the silver is spatially distributed as clusters within the ligaments and on the ligament surfaces[43]. The tortuosity (the ratio of the meandering pore-channel length to a straight pore-channel) of unannealed np-Au is ~3, as reported elsewhere[44]. The tortuosity should decrease for the annealed np-Au films since coarser pores would reduce meandering and provide a straighter path through the film thickness, which is qualitatively observed in the corresponding cross-sectional views (Figure 2 left panel). We used SEM to evaluate the electrode thickness from FIB-carved thin films cross-sections (Figure 2 left panel) and pore size from image processing of high magnification top-views (Figure 2 right panel). The median pore size (radius) for the samples was 12 – 15 nm for as-dealloyed (unannealed) electrodes and 28 – 40 nm for coarsened (annealed) np-Au electrodes samples. The electrode thicknesses ranged from 250 ± 15 nm to 1,780 ± 30 nm. Finally, the electrochemically-active surface area was determined via anodic oxide stripping method, as previously described[22,24,30]. The increase in surface area for porous electrodes is expressed as *enhancement factor* (EF), which is the ratio of the electrochemically-active surface area to that of planar gold (pl-Au). We used EF as a parameter that combines both the electrode thickness and pore morphology variables, which allows for more efficient analysis of the influence of electrode properties on sensor performance. Table S1 provides further details of electrode characterization.

Sensor Performance at Varying Electrode Morphologies and EFs.

Effective electrode surface area is one of the main parameters that can influence the performance of an electrochemical biosensor[45,46]. Larger effective to geometric surface area ratio (hence, higher the EF) ideally translates into a larger number of capture DNA probes bound to the sensor, and therefore an enhanced probability of probe-target interactions. This has been one of the primary motivators for the sensor community's interest in nanostructured electrodes [26,31]. To that end, we initially investigated if the increase in EF of the np-Au electrodes monotonously improve the sensor performance. Figure 3 shows the

Author Manuscript Author Manuscript Author Manuscript Author Manuscript

aggregate hybridization current change for the two different morphologies with different thicknesses, expressed in terms of their EF values. Independent of the DNA target concentration (250 – 4000 nM), hybridization current change, which determines detection sensitivity, increased with EF up to approximately an EF of 5. However, the sensor performance deteriorated with higher EFs (indicated by decreasing hybridization current observed for both unannealed and annealed electrode morphologies as shown in Figure S3). In addition, around an EF of 12, the sensor displayed the highest resolution in detecting DNA target at different concentrations. We attribute this EF-dependent reduction in sensor performance to transport limitations of DNA probe and/or target DNA into the deeper pore surfaces, which is discussed next.

Electrochemical and Fluorometric Characterization of the Capture Probe Layer.

Since the quality of the DNA probe monolayer (the capture layer) plays a critical role in the sensor performance[47-49], we investigated whether the entire electrochemically-active surface area is functionalized with the DNA probe using relative probe current measurements and fluorometric quantification of electrochemically desorbed and eluted DNA probe (Figure 4). Normally, the relative probe current is expected to increase with the increasing EF (Figure 4C), as a larger surface area should support more MB-labeled DNA. On the contrary, the relative probe current displayed the opposite of the expected trend (Figure 4A), that is, initially a constant value followed by a rapid decrease for the samples with the largest EF (27.9 and 36.1). The amount of DNA desorbed from the samples with different EFs (Figure 4B) was in an agreement with the amount of DNA recovered from each sample (~10 ng/mL to 50 ng/mL) as determined by our previous studies using the same grafting solution concentration (0.5 μM)[32]. In that study, we observed that the amount of surface-bound and unbound DNA amounts strongly depended on the grafting solution concentration, where recovered DNA probe approached 5000 ng/mL for grafting solution concentrations of 8 μM. These results suggest that there is significant hindrance in permeation of DNA probe into the pores. Only a higher concentration gradient between bulk and the pores, attained by high grafting solution concentrations, can drive DNA into the deeper pores. Figure 4C is a composite plot of electrochemical and fluorometric quantification of the DNA probe layer illustrating the significant deviation from the expected linear relationship[32] (shown with a trendline) between the two read-outs. Taken together, the severely reduced efficiency in grafting the electrochemically-active surface at higher EFs likely plays a role in the impaired sensor performance. Since SWV frequency is one of the main parameters that could affect electrochemical measurements[22,50], we next investigate how different frequencies alter DNA probe signal (surrogate for sensor performance).

Influence of SWV Frequency.

For the MB-tagged DNA capture probe, signal-off sensor, the sensor performance can be influenced by a variety of parameters (e.g., capture probe layer density, target concentration, electrochemical testing parameters, etc.). For any given case, the difference between *probe peak current* and *baseline*, referred to as the *relative probe current*, is used as the main criteria for the sensor optimization (Figure 1). The SWV frequency plays an important role in the magnitude of the relative probe current[6,51]. The frequency that allows the participation of the entire DNA capture layer (labeled with MB reporters) in the redox reaction relies on

Author Manuscript Author Manuscript Author Manuscript Author Manuscript

the rate of electron transfer kinetics and ionic transport in and out of the nanostructured film to facilitate the charge transfer. To investigate the influence of SWV frequency on probe peak current and baseline, we captured the DNA relative probe currents for the different samples at a frequency range of 3 to 40 Hz (Figure 5). There is an increase in the relative probe current with increasing frequency for all EFs at lower SWV frequencies. However, the relative probe current significantly decreases for higher frequencies, particularly for the thicker samples (EFs of 27.9 and 36.1). While unannealed np-Au samples (smaller pores) exhibited higher sensitivity to SWV frequency than the annealed np-Au samples (coarser pores), the relative probe currents reached their maximum value in general at mid-frequencies for all samples with a trend of decreasing optimal frequency as electrode EF increased (Figure S4). While ionic transport into the pores, particularly if they are depleted through the electrochemical processes[18,30,52], may play a role in reducing the relative probe current with increasing frequency, the *peak probe current* followed the expected trend of a square root dependence on scan rate (Figure S5), which can be converted from the SWV frequency by multiplying it with the step size. This suggests that the frequencies used here are below the electron transfer rates to obtain sufficient faradaic current from the MB tag and therefore the *baseline current* may be considerably influencing the final relative probe current, as studied next.

Baseline Shifts.

Baseline current shifts often stem from the capacitive currents due to formation and relaxation of the electric double layer (EDL) at the electrode-electrolyte interface, whereas the faradaic currents are due to redox reactions contributing to the peaks in voltammograms[50,51,53-57]. In order to evaluate the extent of baseline shifts as function of frequency in a stepwise manner, we studied how the baselines evolve as a bare electrode is successively functionalized with MCH and subsequently with the DNA probe with the MB redox reporter (Figure 6 and Figures S6-S8). The first general observation is that the baseline current increases with frequency and with electrode EF. The role of MCH in reducing the baseline shift, plausibly by suppressing EDL, is highlighted by the contrast between bare (Figure 6A) and MCH-functionalized electrodes (Figure 6B). MCH is a short mercapto-alkane molecule that reduces interfacial capacitance[47,58] and reduces non-specific interactions of the electrode and electrolyte[33,59]. The electrodes functionalized with only MCH (Figure 6B) or MCH+DNA exhibit almost identical baseline shift behavior with respect to the frequency (Figure 6C) indicating that MCH passivation of the electrode surfaces is similar for both cases and it is the MCH functionalization (not DNA probe) that dictates the baseline shift. Taken together, the MCH treatment is critical in mitigating the undesirable contribution of capacitive currents, which ultimately reduces the resulting relative peak current (surrogate for sensor performance). However, while the MCH treatment helps in augmenting the relative peak current, the electrodes with high EFs still suffer from large capacitive currents resulting in severely diminished relative peak currents, which negatively impact sensor performance (Figure 3 and 5). This incomplete suppression of the baseline may be in part due to partial passivation of electrochemically-active surfaces especially for thick unannealed np-Au electrodes that are subject to hindered transport of MCH to the deeper pores.

Author Manuscript Author Manuscript Author Manuscript Author Manuscript

Electrochemical Impedance Spectroscopy.

To understand the extent of MCH passivation and its effect on the sensor performance, we conducted electrochemical impedance spectroscopy (EIS) on bare and MCH-functionalized electrodes for the samples with the smallest and largest EF values (Figure S9). We utilized a Randles equivalent circuit with a Warburg element to account for the influence of mass transport within the porous electrode[60-63]. However, the main circuit element of interest in this study is the EDL capacitance (C_{dl}), which should be suppressed upon MCH immobilization as discussed in the previous section [63,64]. The equivalent circuit yields a solution resistance R_s of ~300 Ω across all electrode types, in agreement with PBS resistance reported by others[65,66]. Furthermore, EDL capacitance for the thin, annealed bare np-Au electrode (EF = 3.1) was 25-fold less than that for the thick, unannealed bare sample (EF = 36.1), 24 ± 1 μF and 610 ± 70 μF respectively. Upon MCH passivation, the interfacial capacitance decreased between 75% to 90% with respect to the bare electrodes. This large percent reduction in capacitance rules out the hypothesis that MCH immobilization on thicker electrodes with small pores (i.e., large EF) is prone to hindered transport of MCH and hence partial MCH passivation. Nevertheless, the large effective surface area of thick electrodes still leads to large total interfacial capacitances, hence, more drastic shifts in the baseline current (Figure 6) and consequently a reduced relative probe current (impaired sensor performance) especially for high SWV frequencies. These results further highlight the imperative to identify the break-even electrode film thickness and morphology (bundled into the EF parameter) to maximize the probability of target DNA capture while minimizing mass transport limitations and parasitic capacitive current contributions, all of which increase with higher EFs yet at different rates.

Real-time Target Hybridization.

The observations so far support our initial statement that simply increasing the effective surface area does not translate into enhanced affinity-based electrochemical sensor performance. A variety of behaviors, such as baseline shifts and hindered DNA probe permeation into deeper pore layers, need to be considered. As a corollary to the mass transport limitations for DNA probe grafting,- we leverage the MB-tagged DNA probe capture layer for a real-time study of hybridization kinetics when target DNA is added to the electrochemical cell. Electrodes with different EFs were exposed to three different target concentrations to cover a wide dynamic range (250 nM to 4000 nM) and the time-course up to 15 minutes of hybridization was acquired via monitoring the *hybridization current change*. Figure 7 shows the normalized hybridization current change (normalized to the average of last three timepoints for each group; Figure S10) for two extreme EFs (3.1 and 12.8). Note that we used the sample with EF of 12.8 as the upper bound, since EFs beyond 12.8 suffered from excessive baseline shift with suppressed relative probe current. With increasing DNA target concentration, the steady-state hybridization current change increased for all electrode types (Figures S10), which is expected from the steeper concentration gradient between the bulk and intra-pore volumes likely increasing the permeation of target DNA into the pores. A comparison of the hybridization kinetics (assessed by time to reach the ~50% of steady-state hybridization current change in Figures 7A and 7B) reveals that both np-Au electrodes (EFs of 3.1 and 12.8) respond to added target DNA within a similar time scale (a few minutes) while the pl-Au reaches ~80% of the steady-state hybridization

Author Manuscript Author Manuscript Author Manuscript Author Manuscript

current change during the same duration. This is expected since the target DNA needs to permeate the porous electrode unlike the pl-Au electrode with a flat surface. Moreover, since the bulk diffusion distance for the target DNA onto the electrode surface is the same for np-Au and pl-Au electrodes, the rapid stabilization of pl-Au sensor performance suggests that the rate-limiting transport step is the pore permeation, and not bulk diffusion, underlining the importance of the working electrode properties.

Importantly, the highest steady-state hybridization current change is achieved for EFs around 5 (Figure 7C), underscoring the non-monotonous dependence of sensor performance with respect to the increasing effective surface area. Put another way, it is clear that expanding the effective surface area improves the sensor performance (higher steady-state hybridization current change); however, past a certain EF (~5 for the experimental parameters here), the sensor performance deteriorates and reaches a plateau. Since the majority of the target DNA detection occurs within the top portions of the electrodes, the putative changes in tortuosity due to coarsening may play a minor role in the sensor performance.

CONCLUSIONS

This study demonstrates the interplay of effective surface area (EF), mass transport, and electrochemical features of nanoporous thin film electrode coatings in defining the overall sensor performance. Higher EFs, given undeterred mass transport to the DNA probe capture layer, are desired for maximizing probability of target DNA capture, which enhances sensor sensitivity and response time. However, for porous electrodes, while the EF increases with thickness, the accessibility to the surfaces is hindered by transport limitations. One example of this in the current study was the limit to the amount of DNA probe immobilization that was insensitive to the porous electrode EF. To that end, there is a need for novel working electrode architectures that can both maintain high effective surface area and unhindered access to the surfaces. In addition, the electrodes with higher EF was susceptible to large interfacial capacitance even though partially suppressed by MCH molecules that were less affected by transport limitations due to their small molecular size. The large interfacial capacitance (observed as SWV baseline shifts) ultimately reduced the signal-to-noise ratio of faradaic current to capacitive baseline current, which adversely affected the sensor performance. Finally, the real-time hybridization assay highlighted that the steady-state hybridization current change exhibited a non-monotonous dependence on electrode EF, where increased EF (up to ~5) enhanced sensor performance while larger EFs impaired the performance. Collectively, these observations underline the importance of determining optimal nanostructured electrode thickness and morphology (conveniently expressed as EF) for tapping the optimal sensor performance for nanoporous electrodes. We expect this study to inform the design and implementation of other nanoporous working electrode coatings for advanced electrochemical sensors.

Supplementary Material

Refer to Web version on PubMed Central for supplementary material.

Author Manuscript Author Manuscript Author Manuscript Author Manuscript

ACKNOWLEDGMENT

We acknowledge funding from National Science Foundation (CBET-1512745, CBET&DMR-1454426), National Institutes of Health (R21-EB024635 and R21-AT01093), and University of California - Davis Comprehensive Cancer Center and Microbiome Special Research Program funds. We thank Gregory P Girardi for assistance with sample fabrication, Ryan R Anderson for assistance with sample cross-sections via FIB/SEM imaging, Rabia Mercimek and Melike Tas for SEM image analysis, and Barath Palanisamy for assistance with visualizations.

REFERENCES

(1). Ronkainen NJ; Halsall HB; Heineman WR Electrochemical Biosensors. Chem. Soc. Rev 2010, 39 (5), 1747–1763. [PubMed: 20419217]

(2). Zhang D; Liu Q Biosensors and Bioelectronics on Smartphone for Portable Biochemical Detection. Biosens. Bioelectron 2016, 75, 273–284. [PubMed: 26319170]

(3). Ding X; Srinivasan B; Tung S Development and Applications of Portable Biosensors. J. Lab. Autom 2015, 20 (4), 365–389. [PubMed: 25878051]

(4). Ricci F; Plaxco KW E-DNA Sensors for Convenient, Label-Free Electrochemical Detection of Hybridization. Microchim. Acta 2008, 163 (3–4). 149–155.

(5). Kim J; Campbell AS; de Ávila BEF; Wang J Wearable Biosensors for Healthcare Monitoring Nature Biotechnology. Nature Publishing Group 4 1, 2019, pp 389–406.

(6). Pellitero MA; Shaver A; Arroyo-Currás N Critical Review—Approaches for the Electrochemical Interrogation of DNA-Based Sensors: A Critical Review. J. Electrochem. Soc 2020,167 (3), 037529.

(7). Mohammed MI; Desmulliez MPY Lab-on-a-Chip Based Immunosensor Principles and Technologies for the Detection of Cardiac Biomarkers: A Review. Lab on a Chip. 2011, pp 569–595. [PubMed: 21180774]

(8). Lotfi Zadeh Zhad HR; Lai RY Hexavalent Chromium as an Electrocatalyst in DNA Sensing. Anal. Chem 2017, 89 (24), 13342–13348. [PubMed: 29143529]

(9). Arroyo-Currás N; Somerson J; Vieira PA; Ploense KL; Kippin TE; Plaxco KW Real-Time Measurement of Small Molecules Directly in Awake, Ambulatory Animals. Proc. Natl. Acad. Sci. U. S. A 2017, 114 (4). 645–650. [PubMed: 28069939]

(10). Salimian R; Kékedy-Nagy L; Ferapontova EE Specific Picomolar Detection of a Breast Cancer Biomarker HER-2/Neu Protein in Serum: Electrocatalytically Amplified Electroanalysis by the Aptamer/PEG-Modified Electrode. ChemElectroChem 2017, 4 (4), 872–879.

(11). Lin M; Song P; Zhou G; Zuo X; Aldalbahi A; Lou X; Shi J; Fan C Electrochemical Detection of Nucleic Acids, Proteins, Small Molecules and Cells Using a DNA-Nanostructure-Based Universal Biosensing Platform. Nat. Protoc 2016, 11 (7), 1244–1263. [PubMed: 27310264]

(12). Goodchild J Conjugates of Oligonucleotides and Modified Oligonucleotides: A Review of Their Synthesis and Properties. Bioconjugate Chemistry. 1990, pp 165–187. [PubMed: 1965782]

(13). Song S; Wang L; Li J; Fan C; Zhao J Aptamer-Based Biosensors. TrAC - Trends Anal. Chem 2008 27(2). 108–117.

(14). Daniel S; Rao TP; Rao KS; Rani SU; Naidu GRK; Lee HY; Kawai T A Review of DNA Functionalized/Grafted Carbon Nanotubes and Their Characterization. Sensors and Actuators B-Chemical 2007, 122 (2). 672–682.

(15). Gasparac R; Taft BJ; Lapierre-Devlin MA; Lazareck AD; Xu JM; Kelley SO Ultrasensitive Electrocatalytic DNA Detection at Two- and Three-Dimensional Nanoelectrodes. J. Am. Chem. Soc 2004,126 (39), 12270–12271. [PubMed: 15453752]

(16). Bin XM; Sargent EH; Kelley SO Nanostructuring of Sensors Determines the Efficiency of Biomolecular Capture. Anal. Chem 2010, 82 (14). 5928–5931. [PubMed: 20568723]

(17). Soleymani L; Fang ZC; Sargent EH; Kelley SO Programming the Detection Limits of Biosensors through Controlled Nanostructuring. Nat. Nanotechnol 2009, 4 (12), 844–848. [PubMed: 19893517]

(18). Park S; Kim HC; Chung TD Electrochemical Analysis Based on Nanoporous Structures. Analyst 2012,137(17), 3891–3903. [PubMed: 22774000]

Author Manuscript Author Manuscript Author Manuscript Author Manuscript

(19). Joo S; Park S; Chung TD; Kim HC Integration of a Nanoporous Platinum Thin Film into a Microfluidic System for Non-Enzymatic Electrochemical Glucose Sensing. Anal. Sci 2007, 23 (3), 277–281. [PubMed: 17372368]

(20). Das J; Ivanov I; Montermini L; Rak J; Sargent EH; Kelley SO An Electrochemical Clamp Assay for Direct, Rapid Analysis of Circulating Nucleic Acids in Serum. Nat. Chem 2015, 7 (7), 569–575. [PubMed: 26100805]

(21). Lord H; Kelley SO Nanomaterials for Ultrasensitive Electrochemical Nucleic Acids Biosensing. J. Mater. Chem 2009,19 (20), 3127–3134.

(22). Daggumati P; Matharu Z; Seker E Effect of Nanoporous Gold Thin Film Morphology on Electrochemical DNA Sensing. Anal. Chem 2015, 87 (16). 8149–8156. [PubMed: 25892217]

(23). Haverkort JW A Theoretical Analysis of the Optimal Electrode Thickness and Porosity. Electrochim. Acta 2019, 295, 846–860.

(24). Matharu Z; Daggumati P; Wang L; Dorofeeva TS; Li ZD; Seker E Nanoporous-Gold-Based Electrode Morphology Libraries for Investigating Structure-Property Relationships in Nucleic Acid Based Electrochemical Biosensors. ACS Appl. Mater. Interfaces 2017, 9 (15), 12959–12966. [PubMed: 28094510]

(25). Veselinovic J; Li Z; Daggumati P; Seker E Electrically Guided DNA Immobilization and Multiplexed DNA Detection with Nanoporous Gold Electrodes. Nanomaterials 2018, 8 (5).

(26). Daggumati P; Matharu Z; Wang L; Seker E Biofouling-Resilient Nanoporous Gold Electrodes for DNA Sensing.. Anal. Chem 2015, 87 (17), 8618–8622. [PubMed: 26274576]

(27). Şeker E; Shih WC; Stine KJ Nanoporous Metals by Alloy Corrosion: Bioanalytical and Biomedical Applications. MRS Bull. 2018.

(28). Daggumati P; Kurtulus O; Chapman CAR; Dimlioglu D; Seker E Microfabrication of Nanoporous Gold Patterns for Cell-Material Interaction Studies. Jove-Journal Vis. Exp 2013, 77 (77).

(29). Dorofeeva TS; Seker E In Situ Electrical Modulation and Monitoring of Nanoporous Gold Morphology. Nanoscale 2016, 8 (47), 19551–19556. [PubMed: 27790649]

(30). Tan YH; Davis JA; Fujikawa K; Ganesh NV; Demchenko AV; Stine KJ Surface Area and Pore Size Characteristics of Nanoporous Gold Subjected to Thermal, Mechanical, or Surface Modification Studied Using Gas Adsorption Isotherms, Cyclic Voltammetry, Thermogravimetric Analysis, and Scanning Electron Microscopy. J. Mater. Chem 2012, 22, 6733–6745. [PubMed: 22822294]

(31). Patel J; Radhakrishnan L; Zhao B; Uppalapati B; Daniels RC; Ward KR; Collinson MM Electrochemical Properties of Nanostructured Porous Gold Electrodes in Biofouling Solutions. Anal. Chem 2013 85 (23). 11610–11618. [PubMed: 24245771]

(32). Veselinovic J; Almashtoub S; Seker E Anomalous Trends in Nucleic Acid-Based Electrochemical Biosensors with Nanoporous Gold Electrodes. Anal. Chem 2019 91 (18). 11923–11931. [PubMed: 31429540]

(33). Levicky R; Herne TM; Tarlov MJ; Satija SK Using Self-Assembly to Control the Structure of DNA Monolayers on Gold: A Neutron Reflectivity Study. J. Am. Chem. Soc 1998 120 (38). 9787–9792.

(34). Lao R; Song S; Wu H; Wang L; Zhang Z; He L; Fan C Electrochemical Interrogation of DNA Monolayers on Gold Surfaces. Anal. Chem 2005 77(19). 6475–6480. [PubMed: 16194115]

(35). Campuzano S; Yáñez-Sedeño P; Pingarrón JM Tailoring Sensitivity in Electrochemical Nucleic Acid Hybridization Biosensing: Role of Surface Chemistry and Labeling Strategies. ChemElectroChem 2019 6(1). 60–72.

(36). Fan C; Plaxco KW; Heeger AJ Electrochemical Interrogation of Conformational Changes as a Reagentless Method for the Sequence-Specific Detection of DNA. Proc. Natl. Acad. Sci. U. S. A 2003, 100 (16), 9134–9137. [PubMed: 12867594]

(37). Daggumati P; Appelt S; Matharu Z; Marco ML; Seker E Sequence-Specific Electrical Purification of Nucleic Acids with Nanoporous Gold Electrodes. J. Am. Chem. Soc 2016, 138 (24), 7711–7717. [PubMed: 27244455]

Author Manuscript Author Manuscript Author Manuscript Author Manuscript

(38). Veselinovic J; Alangari M; Li Y; Matharu Z; Artés JM; Seker E; Hihath J Two-Tiered Electrical Detection, Purification, and Identification of Nucleic Acids in Complex Media. Electrochim. Acta 2019, 313, 116–121.

(39). Wang J; Rivas G; Jiang M; Zhang X Electrochemically Induced Release of DNA from Gold Ultramicroelectrodes. Langmuir 1999,15 (19), 6541–6545.

(40). Takeishi Shunsaku, Rant Ulrich, Fujiwara Tsuyoshi, Buchholz Karin, Usuki Tatsuya, Arinaga Kenji, Takemoto Kazuya, Yamaguchi Yoshitaka, Tornow Marc, Fujita Shozo, Abstreiter Gerhard, Yokoyama, N. Observation of Electrostatically Released DNA from Gold Electrodes with Controlled Threshold Voltages. J. Chem. Phys 2004, 120 (12), 5501–5504. [PubMed: 15267424]

(41). Erlebacher J; Aziz MJ; Karma A; Dimitrov N; Sieradzki K Evolution of Nanoporosity in Dealloying. Nature 2001, 410 (6827), 450–453. [PubMed: 11260708]

(42). Chapman CAR; Chen H; Stamou M; Biener J; Biener MM; Lein PJ; Seker E Nanoporous Gold as a Neural Interface Coating: Effects of Topography, Surface Chemistry, and Feature Size. ACS Appl. Mater. Interfaces 2015 7(13). 7093–7100. [PubMed: 25706691]

(43). Mahr C; Kundu P; Lackmann A; Zanaga D; Thiel K; Schowalter M; Schwan M; Bals S; Wittstock A; Rosenauer A Quantitative Determination of Residual Silver Distribution in Nanoporous Gold and Its Influence on Structure and Catalytic Performance. J. Catal 2017, 352, 52–58.

(44). Xue Y; Markmann J; Duan H; Weissmüller J; Huber P Switchable Imbibition in Nanoporous Gold. Nat. Commun 2014, 5 (4237), 1–8.

(45). Tan A; Lim C; Zou S; Ma Q; Gao Z Electrochemical Nucleic Acid Biosensors: From Fabrication to Application. Anal. Methods 2016, 26 (8). 5169–5189.

(46). Wang J Electrochemical Nucleic Acid Biosensors. Anal. Chim. Acta 2002 469(1), 63–71.

(47). Steel AB; Levicky RL; Herne TM; Tarlov MJ Immobilization of Nucleic Acids at Solid Surfaces: Effect of Oligonucleotide Length on Layer Assembly. Biophys. J 2000, 79 (2), 975–981. [PubMed: 10920027]

(48). Rashid JIA; Yusof NA The Strategies of DNA Immobilization and Hybridization Detection Mechanism in the Construction of Electrochemical DNA Sensor: A Review. Sensing and Bio-Sensing Research. 2017, pp 19–31.

(49). Nimse SB; Song K; Sonawane MD; Sayyed DR; Kim T Immobilization Techniques for Microarray: Challenges and Applications. Sensors (Switzerland) 2014 14 (12). 22208–22229.

(50). Ricci F; Lai RY; Heeger AJ; Plaxco KW; Sumner JJ Effect of Molecular Crowding on the Response of an Electrochemical DNA Sensor. Langmuir 2007, 23 (12), 6827–6834. [PubMed: 17488132]

(51). Dauphin-Ducharme P; Plaxco KW Maximizing the Signal Gain of Electrochemical-DNA Sensors. Anal. Chem 2016, 88 (23), 11654–11662. [PubMed: 27805364]

(52). Xiao XX; Si PC; Magner E An Overview of Dealloyed Nanoporous Gold in Bioelectrochemistry. Bioelectrochemistry 2016, 109, 117–126. [PubMed: 26781363]

(53). Holtan MD; Somasundaram S; Khuda N; Easley CJ Nonfaradaic Current Suppression in DNA-Based Electrochemical Assays with a Differential Potentiostat. Anal. Chem 2019, 91 (24), 15833–15839. [PubMed: 31718147]

(54). Kang D; Ricci F; White RJ; Plaxco KW Survey of Redox-Active Moieties for Application in Multiplexed Electrochemical Biosensors. Anal. Chem 2016, 88 (21), 10452–10458. [PubMed: 27659949]

(55). White RJ; Phares N; Lubin AA; Xiao Y; Plaxco KW Optimization of Electrochemical Aptamer-Based Sensors via Optimization of Probe Packing Density and Surface Chemistry. Langmuir 2008, 24 (18), 10513–10518. [PubMed: 18690727]

(56). Somasundaram S; Holtan MD; Easley CJ Understanding Signal and Background in a Thermally Resolved, Single-Branched DNA Assay Using Square Wave Voltammetry. Anal. Chem 2018, 90 (5), 3584–3591. [PubMed: 29385341]

(57). Wang J Analytical Electrochemistry. Third Edition; 2006.

(58). Arinaga K; Rant U; Tornow M; Fujita S; Abstreiter G; Yokoyama N The Role of Surface Charging during the Coadsorption of Mercaptohexanol to DNA Layers on Gold: Direct

Author Manuscript Author Manuscript Author Manuscript Author Manuscript

Observation of Desorption and Layer Reorientation. Langmuir 2006, 22 (13), 5560–5562. [PubMed: 16768474]

(59). Herne TM; Tarlov MJ Characterization of DNA Probes Immobilized on Gold Surfaces. J. Am. Chem. Soc 1997, 119 (38), 8916–8920.

(60). Cooper SJ; Bertei A; Finegan DP; Brandon NP Simulated Impedance of Diffusion in Porous Media. Electrochim. Acta 2017, 251, 681–689.

(61). Jurczakowski R; Hitz C; Lasia A Impedance of Porous Au Based Electrodes. J. Electroanal. Chem 2004, 572 (2), 355–366.

(62). Raistrick ID Impedance Studies of Porous Electrodes. Electrochim. Acta 1990 35 (10). 1579–1586.

(63). Huang KC; White RJ Random Walk on a Leash: A Simple Single-Molecule Diffusion Model for Surface-Tethered Redox Molecules with Flexible Linkers. J. Am. Chem. Soc 2013 135 (34). 12808–12817. [PubMed: 23919821]

(64). Yang W; Lai RY Comparison of the Stem-Loop and Linear Probe-Based Electrochemical DNA Sensors by Alternating Current Voltammetry and Cyclic Voltammetry. Langmuir 2011, 27 (23), 14669–14677. [PubMed: 21981414]

(65). Johnson AM; Sadoway DR; Cima MJ; Langer R Design and Testing of an Impedance-Based Sensor for Monitoring Drug Delivery. J. Electrochem. Soc 2005, 152 (1), H6.

(66). Chaparro CV; Herrera LV; Meléndez AM; Miranda DA Considerations on Electrical Impedance Measurements of Electrolyte Solutions in a Four-Electrode Cell. J. Phys. Conf. Ser 2016, 687 (1).

Author Manuscript Author Manuscript Author Manuscript Author Manuscript

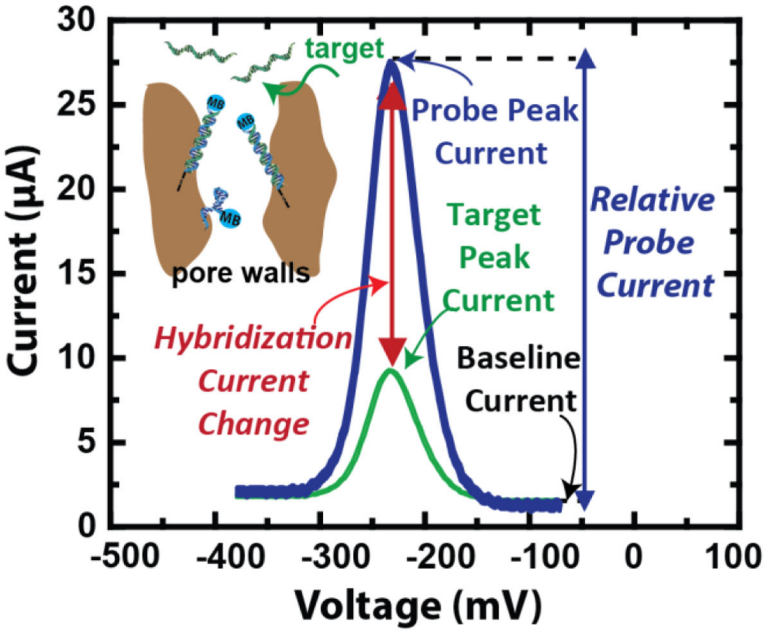

Figure 1.

Description of electrochemical sensor read-out terminology for the *signal-off* DNA detection mode.

Author Manuscript Author Manuscript Author Manuscript Author Manuscript

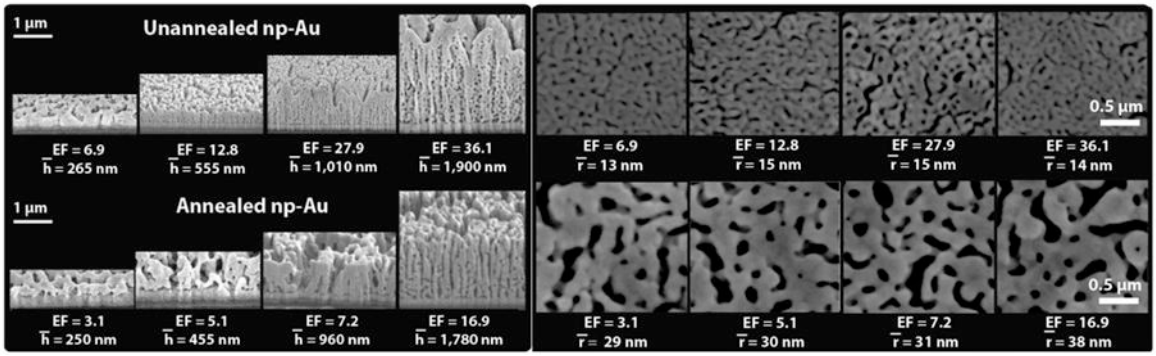

Figure 2.

Left Panel: FIB/SEM micrographs of cross-sectional views of unannealed and annealed np-Au films at various surface area enhancement factors (EFs). Right Panel: SEM micrographs of top-view unannealed and annealed np-Au films at various EFs. Electrode thickness (*h*) and pore radius (*r*) displayed for each sample image.

Author Manuscript Author Manuscript Author Manuscript Author Manuscript

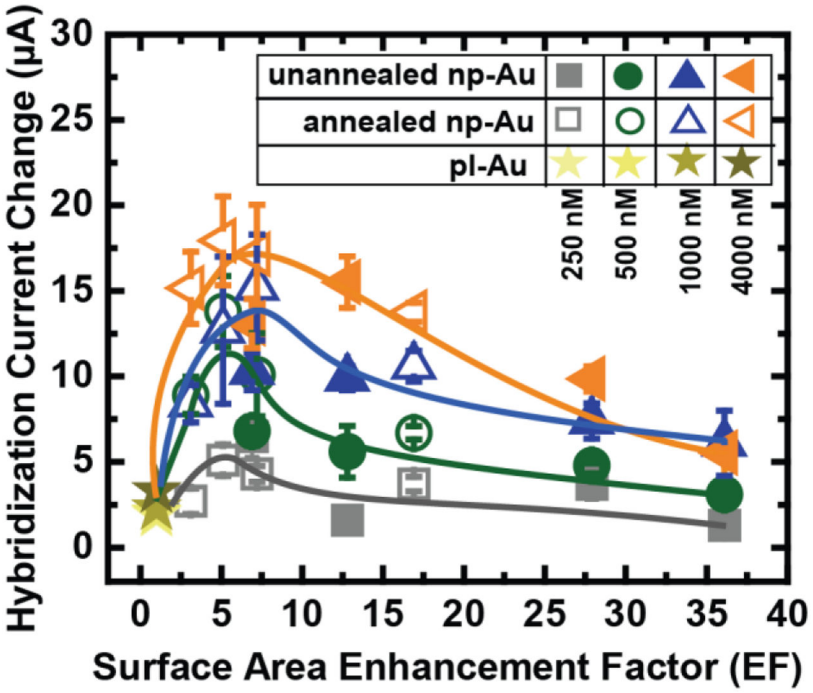

Figure 3.

Hybridization current change for a range of EFs (unannealed np-Au, annealed np-Au, and control pl-Au) when exposed to various target ssDNA concentrations (250, 500, 1000, 4000 nM) illustrating non-monotonic dependence on EF. Trendlines are visual guides only.

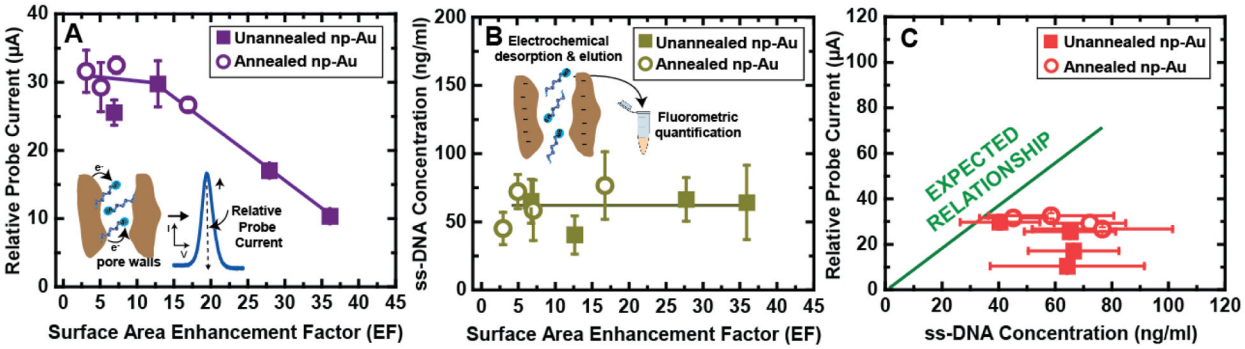

Figure 4.

(A) Electrochemical DNA probe current signal for unannealed and annealed np-Au at varying EFs immobilized with 0.5 μM DNA probe grafting solution concentration; (B) OliGreen fluorometric determination of ss-DNA concentration of the immobilized DNA probe on sample for various EFs and morphologies; (C) Composite plot of (A) and (B) to show the discrepancy between electrochemical and fluorescence measurements in the amount of DNA probe immobilized on the sample surface. Trendlines are visual guides only.

Author Manuscript Author Manuscript Author Manuscript Author Manuscript

Author Manuscript Author Manuscript Author Manuscript Author Manuscript

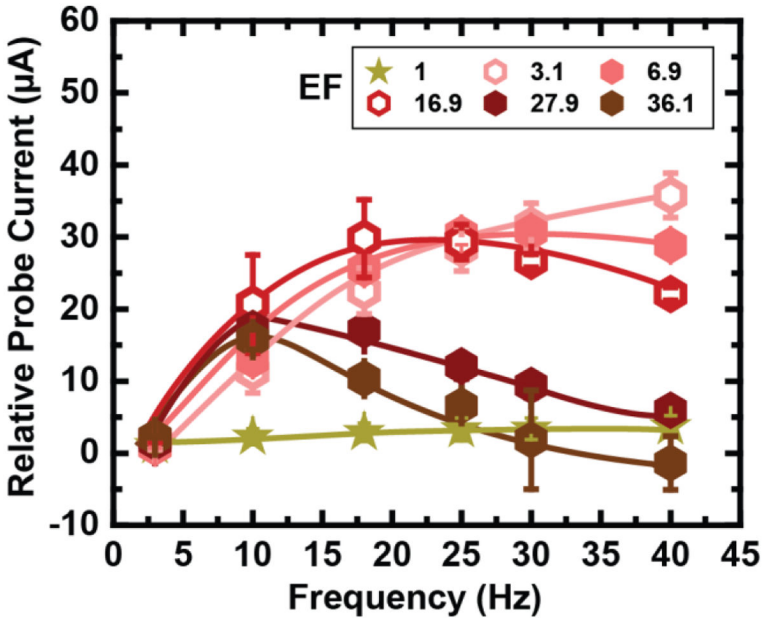

Figure 5.

DNA relative probe current measurements as a function of square wave voltammetry frequency for unannealed np-Au (solid data points), annealed np-Au (open data points) and control pl-Au (star), at their respective EFs. See Figure S5 for all EFs. Trendlines are visual guides only.

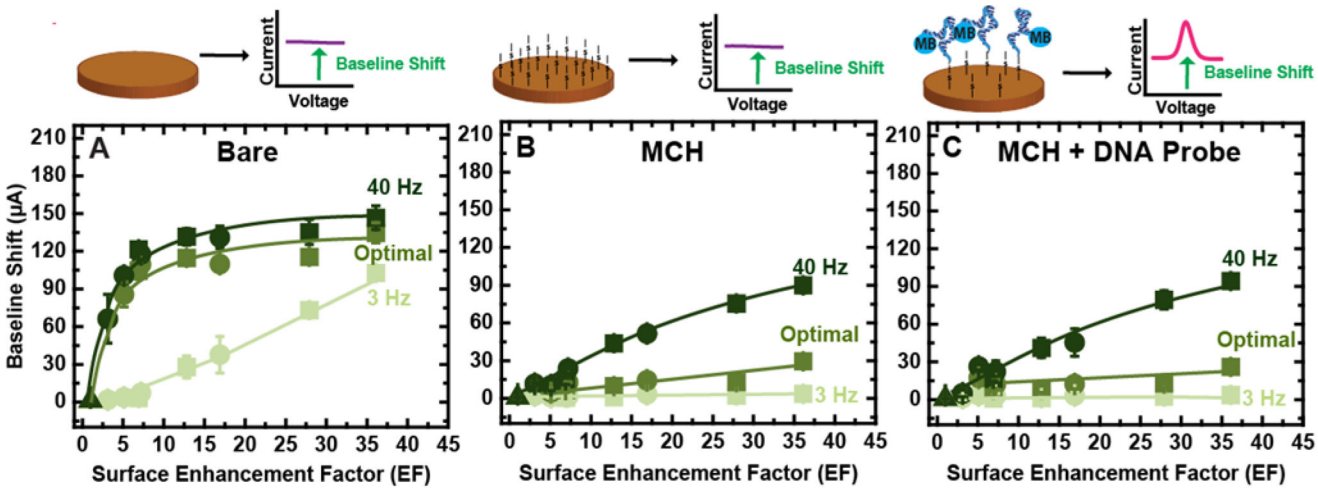

Figure 6.

Baseline shifts with respect to electrode EFs interrogated at various SWV frequencies for successive surface functionalization types (A: Bare electrode; B: MCH functionalization; C: MCH and DNA probe functionalization). Trendlines are visual guides only.

Author Manuscript Author Manuscript Author Manuscript Author Manuscript

Author Manuscript Author Manuscript Author Manuscript Author Manuscript

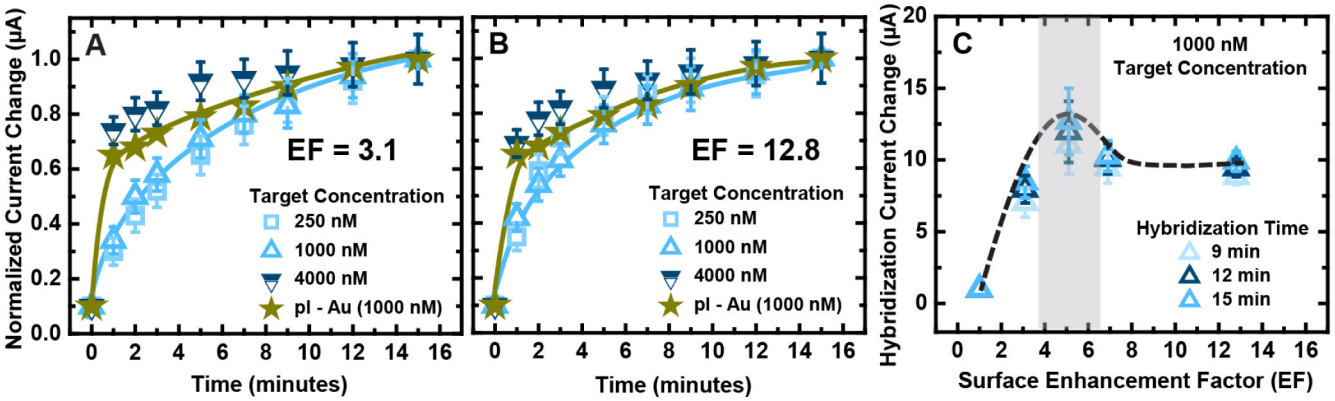

Figure 7.

Normalized hybridization current change for (A) EF = 3.1 and (B) EF = 12.8. for various target concentrations, measured at 1, 2, 3, 5, 7, 9, 12 and 15 minutes. (C) Hybridization current change at t = 9, 12 and 15 minutes for all EFs. Trendlines are visual guides only.